

DENSITY PROFILES IN MOLECULAR CLOUD CORES ASSOCIATED WITH HIGH-MASS STAR-FORMING REGIONS

L. E. Pirogov^{1,*}

¹*Institute of Applied Physics RAS*

Radial density profiles for the sample of dense cores associated with high-mass star-forming regions from southern hemisphere have been derived using the data of observations in continuum at 250 GHz. Radial density profiles for the inner regions of 16 cores (at distances $\lesssim 0.2 - 0.8$ pc from the center) are close on average to the $\rho \propto r^{-\alpha}$ dependence, where $\alpha = 1.6 \pm 0.3$. In the outer regions density drops steeper. An analysis with various hydrostatic models showed that the modified Bonnor-Ebert model, which describes turbulent sphere confined by external pressure, is preferable compared with the logtrope and polytrope models practically in all cases. With a help of the Bonnor-Ebert model, estimates of central density in a core, non-thermal velocity dispersion and core size are obtained. The comparison of central densities with the densities derived earlier from the CS modeling reveals differences in several cases. The reasons of such differences are probably connected with the presence of density inhomogenities on the scales smaller than the telescope beam. In most cases non-thermal velocity dispersions are in agreement with the values obtained from molecular line observations.

1. INTRODUCTION

The knowledge of density structure in star-forming cores is very important for selecting most adequate theoretical models and for understanding the processes which lead to formation of stars from dense gas. Nowadays, there exists a general picture which describes the low-mass star formation process ($M \sim 1 M_{\odot}$) (see, e.g. [1, 2]), whereas the process of star formation in clusters, where high-mass stars ($M \gtrsim 8 M_{\odot}$) are born, is studied much weaker. The cores where low-mass stars are forming are assumed to be initially in hydrostatic

* Electronic address: pirogov@appl.sci-nnov.ru

equilibrium in which gravitational force is in balance with thermal and magnetic pressure. During their evolution the cores lose stability and pass to the state of contraction. For the case when inner pressure is purely thermal whereas central density and radius of the sphere are finite, the stable solutions of hydrostatic equations exist, if the sphere is confined by external pressure (the Bonnor-Ebert model [3, 4]). Recently, a number of papers appeared which confirm that this model well describes the observed column density profiles in dense molecular cloud cores where low-mass stars are forming (see, e.g. [5–7]). Most of the studied objects turn out to be either unstable or near the critical state. Model calculations show that the density distribution corresponding to the Bonnor-Ebert model can remain for unstable objects [7, 8]. Although this model describes isothermal sphere, whereas observations show that there are non-thermal gas motions in the studied objects which lead to additional line broadening, one can take them into account by adding into equation of state the pressure due to non-thermal motions and considering that it is uniform and isotropic (microturbulent approximation) [9]. However, the model described above is not without alternatives. Recently, the gravoturbulent model of star formation, where the observed cores can be unstable density fluctuations in a turbulent cloud, is developed [10]. Nonetheless, density profiles in such cores are close to those followed from the Bonnor-Ebert model [11].

The picture of high-mass star formation in dense cores, where non-thermal turbulent motions prevail upon the thermal ones and evolution is going considerably quicker than in low-mass star-forming regions, is still under construction nowadays. Several theoretical works suggest to use either polytrope models ($P \propto \rho^{1+1/N}$, where P is a pressure, ρ is a density) or phenomenological “logotrope” model [14] ($P/P_c = 1 + A \ln(\rho/\rho_c)$, where P_c and ρ_c are pressure and density in the center, respectively, $A \approx 0.2$) as the equation of state for high-mass star-forming regions. Both logotrope and polytrope equation with $N < -1$ predict an increase of velocity dispersion from center to periphery corresponding to the observed relations between line width and emission region size (see, e.g. [15, 16]). However, a number of observations of high-mass star-forming regions shows that non-thermal gas velocity dispersion is either constant or increases towards the center [16, 17] which also allows to consider polytropes with positive N -index. Note, that both polytrope spheres with $N > 5$ and the spheres with $N < -1$ as well as the Bonnor-Ebert isothermal sphere model have infinite mass and infinite radius, so the stable configurations can exist if they are confined by a pressure from external medium [18]. In order for a sphere to be in equilibrium, a center-to-edge density ratio should

be not higher than 14.3 in the Bonnor-Ebert model (see e.g. [19]) while for the logotrope model the maximum value for this ratio can reach $\gtrsim 100$ [14].

Until now, the Bonnor-Ebert model is used in analysis of the observed gas and dust distributions in the cores where low-mass stars are forming. In the studies of density distributions in the cores associated with high-mass star-forming regions one usually limits himself by the fitting power-law dependences into observational data. If object is in hydrostatic equilibrium, the power-law index of radial density profile written in the form of power-law function ($\rho \propto r^{-\alpha}$) is close to zero in the center and asymptotically tends to 2 (the Bonnor-Ebert model) or to unity (the logotrope model) far from the center. In the polytrope models the α -index on periphery can accept values between 1 and 2 depending on the value of N . Both the logotrope and the polytrope models are not free of drawbacks (see the critique in [13, 14, 20]). This leads to the necessity of considering more complex models [20, 21].

In order to examine the models one needs experimental measurements of density profiles which can be obtained from observations of intensity distributions of optically thin molecular lines, if radial excitation temperature profile is known, or from dust continuum emission if dust temperature profiles and dust absorption coefficient are known. Recently, the methods based on estimates of star color variations in near infrared due to absorption in dust cloud are used to estimate dust column densities [22]. In the present work an analysis of dust continuum maps obtained towards several high-mass star-forming regions [23] is carried out. The density profiles in the cores contained in these regions have been estimated with a help of different models. The results of the analysis are given below.

2. SOURCE SELECTION

The data of observations of the sample of high-mass star-forming regions from southern hemisphere in continuum at 250 GHz [23] have been used to estimate density profiles. The source list with coordinates and distances is given in Table 1.

The observed regions contain one or several intensity peaks which can be associated with dense cores [23]. Two examples of maps of the regions consisted of one and three cores, respectively, are shown in Fig. 1. Parameters of distinct cores are determined by fitting single or multiple Gaussian elliptic distributions convolved with the telescope beam (the values of the axes ratio of the fitted ellipse and the relative coordinates of its center are given in

Table 4 from [23]). As far as the following analysis is performed within the framework of spherically-symmetric model, we have selected 16 cores which emission regions geometry is close to the circular one (the axes ratio of the fitted ellipse does not exceed 2), with total fluxes higher than 5 Jy and with sizes higher or of the order of the main telescope beam (24'') [23]. The iterative Marquard-Levenberg method has been used (see e.g. [28]) for fitting model distributions convolved with the beam into the observed maps. The values of model parameters and their uncertainties have been determined on its basis.

3. THE ANALYSIS WITH POWER-LAW FUNCTIONS

As far as the sources are optically thin at the frequency of observations (ν), the intensity of their emission can be given by the following integral along the line of sight (see e.g. [29]):

$$I_\nu = \int B_\nu[T(l)] \rho(l) k_\nu dl \quad (1)$$

where $B_\nu[T(l)]$ is the Plank function, $T(l)$ is a dust temperature, $\rho(l)$ is a density, k_ν is a dust absorption coefficient. The convolution of I_ν with the telescope beam gives the observed intensities. If dust temperature along the line of sight is constant and the properties of dust grains are also constant ($k_\nu = const$), the observed intensities are proportional to dust and gas column densities (given that the gas-to-dust mass ratio is constant) in the column having cross-sectional area equal to the projection of the main beam.

If one approximates density profile in the cores by power-law function, it is possible to estimate its power-law index from observational data. For this purpose a two-dimensional power-law function with arbitrary power-law index (b^{-p} , where b is a projected distance from the center of map) convolved with the beam has been fitted into the maps of the cores. An amplitude of the fitting function, a value of additive constant term, coordinates of a center and power-law index p are varied in order to get minimum of discrepancy. As far as a function with single power-law index p leads to unsatisfactory results in most cases (below, in Fig. 2 the results of fitting by such a function is shown by dots for G268.42), it has been replaced by composite power-law function for which power-law indices in inner and outer core regions are different. The value of division radius between these regions is varied to get minimum of discrepancy. The values of power-law indices for inner and outer regions (p_i and p_{out} , respectively) as well as angular and linear values of division radius between these regions

are given in Table 2. Uncertainties derived from the fitting are given in brackets. The cores that belong to the same region are marked by numbers. Their numbering is taken from [23]. In addition, G291.27(4) with relative coordinates (182'', 34'') is included into the list. For two cores in G316.77 and for G345.01(2) the results of fitting by power-law function with single power-law index for the whole core and convolved with the telescope beam are given (the p_i and p_{out} values are the same for them). A presence or an absence of the IRAS source within the core is indicated in the last column of the table. The examples of the observed intensities and fitted functions for eight sample cores are shown in Fig. 2 as one-dimensional dependences on the distance from core center.

If dust properties do not vary with radius at least for inner regions of the cores, the power-law index for radial density profile can be obtained from the following relation [29]:

$$\alpha \approx p + 1 - Qq \quad (2)$$

where q is a power-law index for dust temperature radial dependence; $Q = (x e^x)/(e^x - 1)$ is a correction factor; $x = h\nu/K_B T$; h and K_B are the Plank and the Boltzmann constants, respectively; ν is a frequency; T is a dust temperature. The q value depends on β , the power-law index of the dependence of dust optical depth on frequency ($q = 2/(\beta + 4)$ [30]). As in [23] the β value is set to 2; in this case $q = 0.33$.

The cores without heating sources are most probably isothermal ($q = 0$). The dust temperatures for the cores with IRAS sources [23] and the α_i values for inner regions of the cores, calculated using these temperatures, are given in Table 2. These values lie in the range 1.1 – 2.2 in accordance with the ranges found by other authors for the samples of high-mass star-forming regions [31–34]. The mean value of α_i is 1.6(0.3). The values of $\langle\alpha_i\rangle$ for the cores with and without IRAS sources are close to each other within the standard deviations given in brackets. They are 1.5(0.3) and 1.8(0.3), respectively. The α_{out} index for the outer regions of the cores is systematically higher than α_i .

4. THE ANALYSIS WITH HYDROSTATIC MODELS

As far as absolute values of power-law indices of radial density profiles in the cores are higher on periphery than in inner regions (see Section 3), it is possible to use the models of hydrostatic equilibrium spheres confined by external pressure for their description. The

power-law index α of the $\rho \propto r^{-\alpha}$ dependence rises with the distance from the center in these models. The molecular line widths observed in the sample cores are considerably higher than the thermal ones [17, 23], therefore, instead of using standard Bonnor-Ebert model one should consider a “modified” model (see e.g. [9]) which includes, apart from the thermal pressure, the pressure from random non-thermal motions. If the latter is homogeneous and isotropic (microturbulent approximation), its contribution can be taken into account as an additional term in the equation of state:

$$P = \rho \left(\frac{kT}{m} + V_{\text{nt}}^2 \right) \approx \rho V_{\text{nt}}^2 \quad (V_{\text{nt}}^2 \gg \frac{kT}{m}), \quad (3)$$

where m is a mean molecular mass, V_{nt} is a mean velocity of non-thermal motions. Density distribution can be obtained using Lane-Emden equation for isothermal sphere:

$$\frac{1}{\xi^2} \frac{d}{d\xi} \left(\xi^2 \frac{d\psi}{d\xi} \right) = e^{-\psi}, \quad (4)$$

where $\psi(\xi) = -\ln(\rho/\rho_c)$, $\xi = r \cdot a$ is a dimensionless radius, $a = V_{\text{nt}}^{-1} \sqrt{4\pi G \rho_c}$, where G is the gravitational constant. The boundary conditions $\psi(0) = 0$, $\psi'(0) = 0$ are used for solving the equation (4).

By solving the equation (4) we obtain density and column density profiles. Having calculated the convolution of column density distribution with the telescope beam and having fitted it into the maps, it is possible to estimate discrepancy according to which increments of the parameters are calculated. An amplitude of the fitted function, an additive constant term, coordinates of the center, a -parameter and radius of a sphere (R_{max}) are varied for each core when model profiles are fitted into the maps. Using the values of amplitude and a -parameter one can calculate V_{nt} and ρ_c . This model, thus, allows to determine such physical parameters as central density, dispersion of turbulent velocities and size of a core. The comparison of the fitting results of the modified Bonnor-Ebert model and composite power-law function (Section 3) has not revealed the preference of any of them according to the value of discrepancy.

The results obtained from applying the modified Bonnor-Ebert model are given in Table 3. Dust temperatures which are need to calculate the Plank function have been taken from [23] (Table 2) for the cores with IRAS sources or have been set to 20 K for the cores without inner sources. The values of central density ($n_c = \rho_c/m$) and corresponding Doppler line width

($\Delta V_{\text{nt}} = \sqrt{8 \ln 2} V_{\text{nt}}$) are given in the columns 2 and 3 of Table 3. Uncertainties calculated from fitting are given in brackets. Actual uncertainties are most probably higher than those given in the table due to uncertainty in dust absorption coefficient and uncertainty in dust temperature for the cores without inner sources. The gas-to-dust mass ratio is set to 100 while dust absorption coefficient at 250 GHz is set to $1 \text{ cm}^2 \text{ g}^{-1}$ [35]. An exact value of this coefficient for our sample cores is unknown. Depending on the evolutionary phase of a core, the absorption coefficient value can vary up to two times on the one or the other side [36]. This uncertainty can lead to the uncertainty in n_c up to two times and to the uncertainty in V_{nt} up to $\sqrt{2}$ times. The $\text{N}_2\text{H}^+(1-0)$ and $\text{CS}(5-4)$ line widths [17, 23] observed towards the core centers are given in Table 3 for comparison. In last two columns the values of R_{max} and $\xi_{\text{max}} = \xi(R_{\text{max}})$ are given. The cores with $\xi_{\text{max}} > 6.5$ are unstable with respect to gravitational collapse [3, 19].

The distributions derived from the polytrope and the logotrope equations of state have been fitted into the maps of several objects obtained with high signal-to-noise ratios. The Lane-Emden equation for the case of polytrope for $N \neq -1$ can be written in the form [21]:

$$\frac{1}{\xi^2} \frac{d}{d\xi} \left(\xi^2 \frac{d\theta}{d\xi} \right) = -\frac{|N+1|}{N+1} \theta^N, \quad (5)$$

where $\xi = r \cdot a$, $a = V_{\text{nt}}^{-1} \sqrt{4\pi G \rho_c (N+1)^{-1}}$.

For the case of logotrope this equation is written in the form:

$$\frac{1}{\xi^2} \frac{d}{d\xi} \left(\xi^2 \frac{d\theta}{d\xi} \right) = \theta^{-1}, \quad (6)$$

where $\xi = r \cdot a$, $a = V_{\text{nt}}^{-1} \sqrt{20\pi G \rho_c}$. For solving the equations (5),(6) the boundary conditions: $\theta(0) = 1$, $\theta'(0) = 0$ are used.

The polytrope models both with negative and positive values of the N index are used for the data analysis. The comparison with the modified Bonnor-Ebert model showed that the latter is preferable than the logotrope model in all cases and than the polytrope models in most cases as it gives lower discrepancy values, yet, in some cases differences are insignificant. In two cases (G 270.26 и G 285.26) an application of the polytrope models with positive N gives somewhat lower discrepancy value than the Bonnor-Ebert model, yet, the differences are too small to confirm reliably the preference of any model. Moreover, these cores are probably not completely resolved in the observations (see Section 5). The physical parame-

ters derived from the polytrope model for these two objects are given in Table 4. To make a final conclusion about the preference of the polytrope models with positive N one needs observations with higher signal-to-noise ratios. The intensity distributions of dust emission and the curves corresponding to different models are shown in Fig. 3 as one-dimensional dependences on the distance from the center for two representative cores.

5. DISCUSSION

Taking into account probable uncertainties of the estimates derived from fitting model distributions into the maps one can make a conclusion that the ΔV_{nt} values correspond to molecular line widths (see Table 3) with exception of G 291.27(1) and, probably, G 316.77(5). In several cases the CS(5–4) line widths are considerably higher than the $\text{N}_2\text{H}^+(1-0)$ ones which cannot apparently be associated with the difference in optical depth [23] but can reflect the difference in non-thermal velocities of gas that effectively emits in each of these lines. It is known that line widths of nitrogen-bearing molecules, such as NH_3 and N_2H^+ , are systematically lower than of the other dense gas tracers, such as CS, HCN, HCO^+ (see, e.g. [37]), which can be connected with chemical differentiation effects. In our case the fact that the ΔV_{nt} value is close to the one or another molecular line width can indicate which molecular distribution better correlates with total gas and dust distribution in given core.

The comparison of central densities obtained from the Bonnor-Ebert model with densities derived from LVG analysis of the CS(5–4) and CS(2–1) intensities for seven sample cores [23] reveals both proximity (G269.11(1) and G294.97(1)) and discrepancy in these values. Note, that model density estimates depend on the CS line intensity ratios on the whole and only weakly depend on intensities itself in the range of kinetic temperatures, densities and column densities typical for the studied objects. In the case of steep density gradients the CS(5–4) and CS(2–1) emission region sizes are different, which can cause differences in density estimates obtained with different spatial resolution. Such gradients probably exist in G270.26 and G285.26 for which densities according to the Bonnor-Ebert model are more than an order of magnitude higher than densities obtained from LVG analysis of the data convolved to the 50'' beam [23]. The sizes of these cores in continuum are close to the main beam size of the antenna pattern and these sources are probably not completely resolved even in continuum observations. Note, that at high densities and low temperatures the

CS abundances can drop due to depletion onto dust grains toward the centers of the cores without inner sources. This effect can underestimate central densities calculated from LVG analysis. However, it is probably not the case for the considered objects which contain inner heating sources. The LVG densities for G268.42 and G291.27(1) appear to be ~ 2 times lower than those derived from the Bonnor-Ebert model which can be connected with the fact that the actual value of dust absorption coefficient is higher than the standard value used for these sources (see Section 4). The density obtained from LVG calculations for G265.14(1) is an order of magnitude higher than the derived from the Bonnor-Ebert model.

It is important to note that the cores associated with high-mass star-forming regions can be inhomogeneous on the scales unresolved by modern instruments (see [38] and references therein). There are implications that enhanced density regions in the sample cores also could not fill the telescope beam [23]. It is possible that an excess of the LVG density upon the density derived from the Bonnor-Ebert model for G265.14(1) is connected with the fact that the CS emission comes from the clumps with enhanced density and low filling factor whereas density profile derived from dust emission is related to the values averaged over the telescope beam.

In general, the cores studied in the present paper appear to look very like hydrostatic Bonnor-Ebert spheres taking into account turbulent pressure, while such physical parameters as central density, velocity dispersion and size of a core calculated from this model do not contradict independent estimates. Note, however, that the ξ_{\max} value is higher than the critical one more than in half cases, implying their instability in the framework of the Bonnor-Ebert model. We found no correlation between a presence or an absence of closely located IRAS source and stability of a core. Although there are indications in literature that the Bonnor-Ebert profiles can also hold for unstable slowly collapsing objects [7, 8], this fact needs further exploration. Note, that model calculations of the structure of turbulent molecular clouds predict an existence of non-equilibrium density fluctuations which density profiles can be close to those followed from the Bonnor-Ebert model, while physical parameters derived from this model considerably differ from those initially given [11]. In order to get definite conclusion is it correct to apply hydrostatic models to the considered objects the observational data with higher signal-to-noise ratios are needed.

6. CONCLUSIONS

The estimates of radial density profiles for the sample of dense cores associated with high-mass star-forming regions from southern hemisphere have been done using the data of observations in continuum at 250 GHz. For this purpose two-dimensional functions are fitted into the observed maps. The function fitted is a convolution of the telescope beam function and dust column density distribution which is set either arbitrary power-law function or the one followed from various hydrostatic models.

An analysis using power-law functions showed that radial density profiles for the inner regions of 16 cores (at distances $\lesssim 0.2 - 0.8$ pc from the center) are close on average to the $\rho \propto r^{-\alpha}$ dependence, where $\alpha = 1.6 \pm 0.3$. In the outer regions density drops steeply.

Among hydrostatic models the modified Bonnor-Ebert model which describes a sphere with thermal and non-thermal (microturbulent) motions confined by external pressure, as well as the polytrope and the logotrope models have been considered. The modified Bonnor-Ebert model gives the best results practically in all cases. With a help of this model the estimates of central density, non-thermal velocity dispersion and core size have been done. The calculated values of central densities lie in the range: $6 \cdot 10^4 - 2 \cdot 10^7 \text{ cm}^{-3}$, non-thermal velocity dispersions expressed in the form of Doppler line widths lie in the range: $2 - 12 \text{ km/s}$, core sizes are $0.24 - 1.05 \text{ pc}$. The comparison of the central densities with the densities obtained from calculations of the CS molecule excitation [23] has been done. The differences in the values revealed in several cases are probably connected with the presence of density inhomogenities on the scales smaller than the telescope beam. The non-thermal velocity dispersions are in agreement with the values obtained from molecular line observations in most cases.

ACKNOWLEDGMENTS

This work has been carried out with a support from RFBR (06-02-16317, 08-02-00628 grants) and from the program "Active Processes and Stochastic Structures in the Universe"

of the Physical Sciences Division of RAS.

1. F.H. Shu, F.C. Adams, and S. Lizano, *Ann. Rev. Astron. and Astrophys.* 25, 23 (1987)
2. C.F. McKee and E.V. Ostriker, *Ann. Rev. Astron. and Astrophys.* 45, 565 (2007)
3. W.B. Bonnor, *Monthly Not. Roy. Astron. Soc.* 116, 351 (1956)
4. R. Ebert, *Zeitschrift für Astrophysik* 37, 217 (1955)
5. J. Alves, C.J. Lada, and E.A. Lada, *Nature* 409, 159 (2001)
6. N.J. Evans II, J.M.C. Rawlings, Y.L. Shirley, and L.G. Mundy, *Astrophys. J.* 557, 193 (2001)
7. R. Kandori, Y. Nakajima, M. Tamura M., et al., *Astron. J.* 130, 2166 (2005)
8. P.C. Myers, *Astrophys. J.* 623, 280 (2005)
9. Sh.-P. Lai, T. Velusamy, W.D. Langer, and T.B.H. Kuiper, *Astron. J.* 126, 311 (2003)
10. J. Ballesteros-Paredes, R. Klessen, M.-M. Mac Low and E. Vazquez-Semadeni, *Protostars and Planets V*, 63, Univ. of Arizona Press (2007)
11. J. Ballesteros-Paredes, R. Klessen, and E. Vazquez-Semadeni, *Astrophys. J.* 592, 188 (2003)
12. P. Maloney, *Astrophys. J.* 334, 761 (1988)
13. C.F. McKee and J.C. Tan, *Astrophys. J.* 585, 850 (2003)
14. D.E. McLaughlin D.E. and R.E. Pudritz, *Astrophys. J.* 469, 194 (1996)
15. R.B. Larson, *Monthly Not. Roy. Astron. Soc.* 194, 809 (1981)
16. P. Caselli and P.C. Myers, *Astrophys. J.* 446, 686 (1995)
17. L. Pirogov, I. Zinchenko, P. Caselli, et al., *Astron. and Astrophys.* 405, 639 (2003)
18. Y.P. Viala and Gp. Horedt, *Astron. and Astrophys.* 33, 195 (1974)
19. W.H. McCrea, *Monthly Not. Roy. Astron. Soc.*, 117, 562 (1957)
20. C.L. Curry and C.F. McKee, *Astrophys. J.* 528, 734 (2000)
21. C.F. McKee C.F. and J.H. Holliman, *Astrophys. J.* 522, 313 (1999)
22. C.J. Lada, J. Alves, and E.A. Lada, *Astrophys. J.* 512, 250 (1999)
23. L. Pirogov, I. Zinchenko, P. Caselli, and L.E.B. Johansson, *Astron. and Astrophys.* 461, 523 (2007)
24. I. Zinchenko, K. Mattila, and M. Toriseva, M., *Astron. and Astrophys. Suppl. Ser.*, 111, 95 (1995)
25. J. Brand, and L. Blitz, *Astron. and Astrophys.* 275, 67 (1993)

26. M. Juvela, *Astron. and Astrophys. Suppl. Ser.* 118, 191 (1996)
27. T. Neckel, *Astron. and Astrophys.* 69, 51 (1978)
28. W.H. Press, S.A. Teukolsky, W.T. Vetterling, and B.P. Flannery B. P., *Numerical Recipes in Fortran 77*, Cambridge Univ. Press (1992)
29. F.C. Adams, *Astrophys. J.* 382, 544 (1991)
30. S.D. Doty and C.M. Leung, *Astrophys. J.* 424, 729 (1994)
31. K.E. Mueller, Y.L. Shirley, N.J. Evans II, and H.R. Jacobson, *Astrophys. J. Suppl. Ser.* 143, 469 (2002)
32. H. Beuther, H., P. Schilke, P., K.M. Menten, et al., *Astrophys. J.* 566, 945 (2002)
33. J. Hatchell and F.F.S. van der Tak, *Astron. and Astrophys.* 409, 589 (2003)
34. S.J. Williams, G.A. Fuller, and T.K. Sridharan, *Astron. and Astrophys.* 434, 257 (2005)
35. V. Ossenkopf and T. Henning, *Astron. and Astrophys.* 291, 943 (1994)
36. F. Motte, P. André, and R. Neri, *Astron. and Astrophys.*, 336, 150 (1998)
37. L. Pirogov, *Astron. and Astrophys.* 348, 600 (1999)
38. L.E. Pirogov and I.I. Zinchenko, *Astron. Reports* 52, 963 (2008)

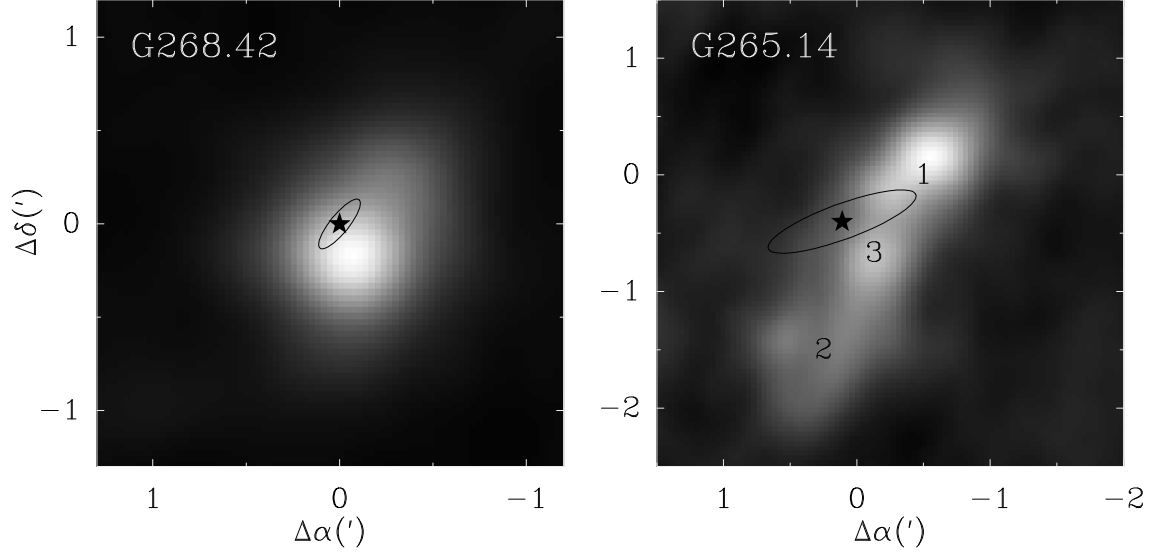


Figure 1. The examples of continuum maps at 250 GHz taken from [23] for two sample objects. The positions of IRAS point sources are indicated by stars. The uncertainties of these positions are indicated by ellipses. Distinct cores for G265.14 are indicated by numbers.

Table 1. Source list

Source	RA (2000)	Dec (2000)	D
	(h) (m) (s)	($^{\circ}$ ' ")	(kpc)
G 265.14+1.45	08 59 24.7	-43 45 22	1.7 [24]
G 268.42-0.85	09 01 54.3	-47 43 59	1.3 [24]
G 269.11-1.12	09 03 32.8	-48 28 39	2.6 [24]
G 270.26+0.83	09 16 43.3	-47 56 36	2.6 [24]
G 285.26-0.05	10 31 30.0	-58 02 07	4.7 [24]
G 291.27-0.71	11 11 49.9	-61 18 14	2.7 [25]
G 294.97-1.73	11 39 12.6	-63 28 47	1.2 [24]
G 316.77-0.02	14 44 58.9	-59 48 29	3.1 [26]
G 345.01+1.80	16 56 45.3	-40 14 03	2.1 [26]
G 351.41+0.64	17 20 53.4	-35 47 00	1.7 [27]

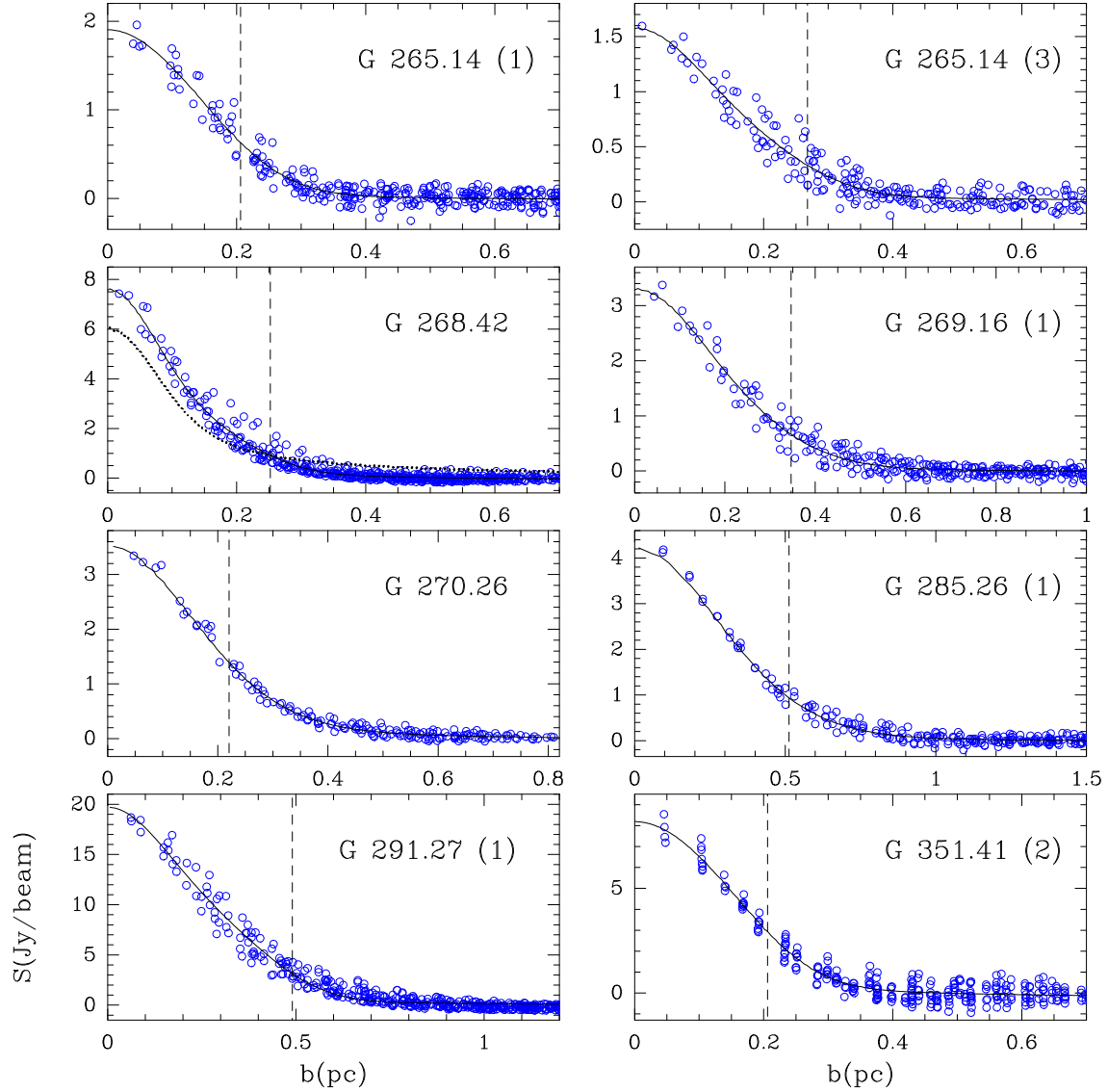


Figure 2. The examples of the observed intensities and fitted two-dimensional model distributions, represented as one-dimensional dependences of flux densities on the distance from the center for eight sample objects. The model distribution is a convolution of composite power-law function and the telescope beam. For G268.42 the result of fitting by a power-law function with single power-law index is shown by dots (an additive constant term is set to zero). Dashed vertical lines denote division radius between inner and outer regions for which power-law indices are different.

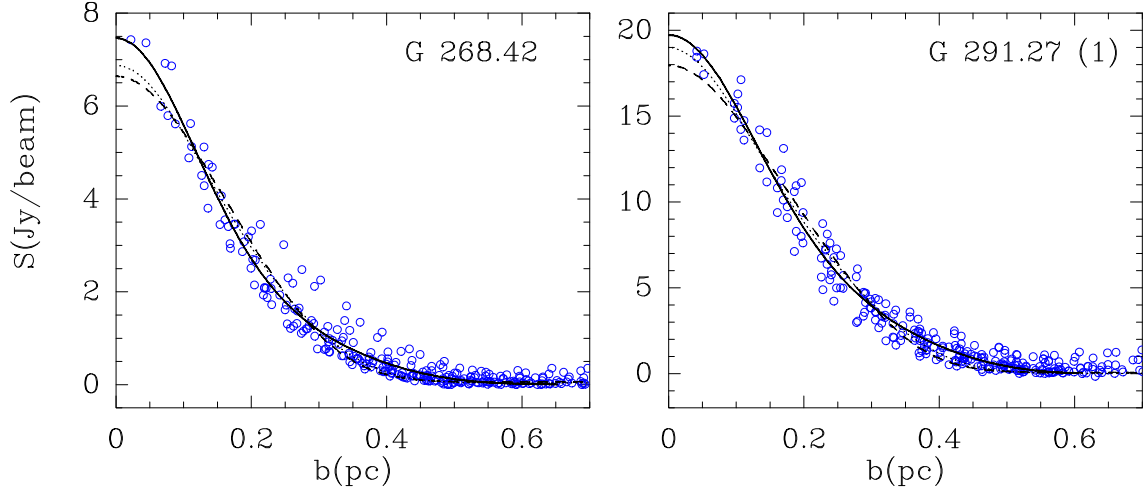


Figure 3. The results of fitting of model distributions into the maps of two cores with highest signal-to-noise ratios. Solid curves correspond to the modified Bonnor-Ebert model, the dashed ones correspond to the logotrope model, the dotted ones correspond to the polytrope model with $N = -2$.

Table 2. The results obtained from fitting by power-law functions

Source	T (K)	p_i	p_{out}	α_i	$\Delta\Theta_S$ (")	R_S (pc)	IRAS
G 265.14+1.45 (1)	30	0.54(0.07)	1.3(0.1)	1.14	25.0	0.21	+
G 265.14+1.45 (2)		0.33(0.05)	0.89(0.08)	1.33	37.5	0.31	-
G 265.14+1.45 (3)	30	0.79(0.05)	1.4(0.1)	1.39	32.5	0.27	+
G 268.42-0.85	35	1.04(0.02)	1.42(0.06)	1.65	40.0	0.25	+
G 269.11-1.12 (1)		1.05(0.04)	1.60(0.08)	2.05	27.5	0.35	-
G 270.26+0.83	29	1.09(0.09)	1.52(0.05)	1.69	17.5	0.22	+
G 285.26-0.05 (1)	33	1.36(0.03)	1.84(0.04)	1.97	22.5	0.51	+
G 291.27-0.71 (1)	25	0.83(0.01)	1.24(0.02)	1.42	37.5	0.49	+
G 291.27-0.71 (3)		0.95(0.06)	1.2(0.3)	1.95	60.0	0.79	-
G 291.27-0.71 (4)		0.50(0.05)	1.5(0.5)	1.50	32.5	0.43	-
G 294.97-1.73 (1)	27	0.72(0.03)	0.97(0.04)	1.31	35.0	0.20	+
G 294.97-1.73 (2)		0.81(0.06)	0.94(0.05)	1.81	30.0	0.17	-
G 316.77-0.02 (4)		0.92(0.17)	0.92(0.17)	1.92			-
G 316.77-0.02 (5)		1.16(0.26)	1.16(0.26)	2.16			-
G 345.01+1.80 (2)		0.56(0.13)	0.56(0.13)	1.56			-
G 351.41+0.64 (2)		0.44(0.07)	1.05(0.08)	1.44	25.0	0.21	-

T (K) is a dust temperature [23], p_i and p_{out} are power-law indices of the fitting functions for inner and outer core regions, respectively, α_i is a power-law index of radial density profile for inner regions, $\Delta\Theta_S$ and R_S are angular and linear separation radius values between inner and outer regions, respectively.

Table 3. The results of using the modified Bonnor-Ebert model

Source	n_c (cm^{-3})	ΔV_{nt} (km/s)	$\Delta V(\text{N}_2\text{H}^+)$ (km/s)	$\Delta V(\text{CS})$ (km/s)	R_{max} (pc)	ξ_{max}	IRAS
G 265.14+1.45 (1)	1.4(0.4) 10^5	3.6(1.3)	2.58(0.04)	2.6(0.1)	0.24(0.02)	3.3(1.2)	+
G 265.14+1.45 (2)	1.6(0.4) 10^5	2.7(0.7)	2.34(0.03)	2.0(0.1)	0.27(0.02)	5.2(1.1)	-
G 265.14+1.45 (3)	5.7(0.9) 10^4	4.3(1.2)	1.95(0.03)	4.3(1.2)	0.36(0.02)	2.7(0.7)	+
G 268.42-0.85	1.9(0.2) 10^6	3.9(0.2)	2.64(0.09)	3.4(0.1)	0.36(0.01)	16.4(0.8)	+
G 269.11-1.12 (1)	1.9(0.5) 10^6	5.2(0.9)	3.23(0.03)	5.8(0.1)	0.52(0.02)	18.4(2.4)	-
G 270.26+0.83	1.6(1.4) 10^7	4.6(2.7)	3.42(0.03)	4.2(0.1)	0.36(0.01)	41.7(16.6)	+
G 285.26-0.05 (1)	2.4(0.6) 10^7	6.4(1.0)	3.09(0.39)	5.0(0.1)	0.67(0.02)	66.3(7.4)	+
G 291.27-0.71 (1)	2.1(0.1) 10^6	11.7(0.4)	2.31(0.15)	5.0(0.2)	0.76(0.01)	12.2(0.4)	+
G 291.27-0.71 (3)	1.2(0.2) 10^5	6.7(1.5)			0.50(0.02)	3.3(0.7)	-
G 291.27-0.71 (4)	2.1(0.2) 10^5	4.1(0.4)	2.29(0.03)	2.9(0.1)	1.05(0.09)	15.4(1.7)	-
G 294.97-1.73 (1)	3.2(0.3) 10^5	2.2(0.1)	2.36(0.04)	2.9(0.3)	0.35(0.01)	12.0(0.8)	+
G 294.97-1.73 (2)	6.2(1.0) 10^5	2.2(0.3)	2.57(0.06)	2.3(0.2)	0.44(0.03)	21.0(2.3)	-
G 316.77-0.02 (4)	1.9(0.5) 10^5	3.4(0.6)	3.31(0.01)	4.0(0.3)	0.80(0.07)	13.6(2.2)	-
G 316.77-0.02 (5)	6.2(1.2) 10^4	6.5(2.1)	3.20(0.01)	3.9(0.3)	0.53(0.03)	2.7(0.9)	-
G 345.01+1.80 (2)	3.4(2.0) 10^5	3.3(1.5)	3.30(0.01)	3.1(0.1)	0.45(0.09)	10.3(3.9)	-
G 351.41+0.64 (2)	1.4(0.3) 10^6	8.0(1.8)	4.38(0.02)	7.7(0.1)	0.28(0.02)	5.4(1.1)	-

n_c is a central density, ΔV_{nt} is a Doppler width corresponding to mean velocity of non-thermal motions, R_{max} is a sphere radius, ξ_{max} is a dimensionless radius.

Table 4. The results of using the polytrope model

Source	N	n_c (cm^{-3})	ΔV_{nt} (km/s)	R_{max} (pc)
G 270.26+0.83	8	3.4(0.5) 10^6	4.8(0.5)	0.58(0.07)
G 285.26-0.05 (1)	15	2.5(0.5) 10^7	7.6(1.0)	0.82(0.02)